PROCEEDINGS, 41st Workshop on Geothermal Reservoir Engineering
Stanford University, Stanford, California, February 22-24, 2016
SGP-TR-209

Laboratory Determination of Fracture Sustainability in EGS Systems

Timothy J. Kneafsey, Seiji Nakagawa, Patrick F. Dobson, Sharon E. Borglin, Marco Voltolini, J. Torquil Smith, Li Yang, Eric L. Sonnenthal

Lawrence Berkeley National Laboratory, Earth and Environmental Sciences, 1 Cyclotron Road, Berkeley, CA, 94720 USA

tjkneafsey@lbl.gov

Keywords: engineered geothermal systems, fracture, dissolution, precipitation, experimental

ABSTRACT

Asperities in a fracture subjected to shear offsets prop the fracture open, and are key to providing permeability necessary for efficient fluid circulation in enhanced geothermal systems (EGS). Changes in these asperities and the resulting permeability over time are controlled by many factors including mineral dissolution and precipitation in the fractures and by mechanical deformation of the asperities and the rock. These factors are functions of the temperature, pressure, fluid chemistry, mineralogy, and stress state of the system.

We conducted laboratory experiments to quantify fracture permeability changes under conditions that could be expected in EGS reservoirs (effective fracture normal stress up to several tens of MPa, temperature up to 250°C). Our objective has been to gain a better understanding of how different rock types, mineral compositions, textures, and fracture surface topography affect the life span of fractures, enabling selection of reservoir rock to optimize long-term fracturing effectiveness. In the current experiments, we used rock samples obtained from a borehole at Brady Hot Springs: a meta-mudstone-volcanic sample from beneath 4800 ft. depth, a rhyolite tuff sample from beneath 3900 ft. depth, and an altered tuff from beneath 2300 ft. depth, and a granite sample from the Stripa mine in Sweden.

For our tests we developed and built a specialized laboratory apparatus that applies normal stress on a disk-shaped rock sample containing an induced offset extensile fracture perpendicular to the core axis. In this apparatus, we flow water through a cylindrical hole in the sample center and then radially through the aperture. We measure the aperture change, fracture permeability, and effluent chemistry. Using this system, we performed extended duration tests (several weeks to several months) to assess differences in the time-dependent changes in permeability. Although the rock samples were from different depths and therefore were naturally subjected to different in-situ effective confining stress and temperature, our experiments were conducted using 20.7 MPa effective stress and at 250°C, with distilled water as the pore fluid (150°C for the granite sample). The different rock types exhibited decreasing fracture aperture, with change slowing with increasing time. These decreases, however, were not sufficient to result in significant changes in the permeability of the fracture for the samples from 4800ft and 3900ft. In contrast, the altered tuff sample from 2300 ft exhibited large reductions in both fracture aperture and permeability in less than 2 weeks from the start of the experiment.

To understand the long-duration fracture compaction experiment, we characterized rock mineralogy and mechanical properties (from P and S-wave velocities), and core-scale mineral density variations resulting from dissolution and precipitation using X-ray CT scans. Before and after the tests we measured the surface profile of both fracture surfaces, to identify preferential mineral precipitation and dissolution sites that can affect the flow paths, as well as mechanical damage. All samples exhibited clear chemical reactions on the fracture surfaces as a result of the experiments. Particularly, the rhyolite ash-flow tuff (2.5 month test) and the lithic tuff (2 week test) samples exhibited large reductions in the rock density around the fluid inlet, indicating significant selective dissolution of the minerals. The chemical changes on the fracture surfaces were localized for the two samples exhibiting little permeability changes. In contrast, the lithic tuff sample showed large reductions in permeability, and exhibited uniformly distributed surfaces alteration.

1. INTRODUCTION

Fracture permeability can be greatly enhanced and sustained if the aperture resulting from shear offsets is large. The aperture life span depends upon the life span of self-propping asperities. The duration of these asperities is a function of temperature, pressure and chemical dissolution, precipitation, and mechanical deformation. Although the importance of shear for sustaining fracture permeability is widely recognized, few experimental studies have been conducted on the evolution of the fracture pore space geometry and resulting changes in the permeability under relevant conditions for a geothermal reservoir.

Our objective is to understand the dependence of different rock types, mineral compositions, and fracture surface textures on the longevity of fracture apertures, so that if possible, selection of reservoir rock can be optimized to reduce or eliminate refracturing. Permeability of induced fractures may be impacted by a number of factors: dilation, wear and brecciation of the wall rock, healing by mineral dissolution, grain size, and mineral replacement (Fetterman and Davatzes, 2011, Roth et al. 2013). Enhanced permeability is exhibited in sheared fractures from dilation (Chen et al, 2000, Fetterman and Davatzes, 2011), and this permeability may also be anisotropic (Auradou et al, 2006, Gentier, 1997, Nemoto et al, 2007). When reactivated by shear, silica or calcite healed fractures tend to undergo brittle dilation, enhancing permeability. Ductile deformation of minerals such as chlorite and smectite may assist debris/grain rotation and reduce dilation during shear, resulting in less permeability enhancement upon fracturing, and even reductions in permeability because of clogged pore space (Davatzes and Hickman, 2010).

Dissolution and precipitation strongly impact long-term performance of a geothermal reservoir and are enhanced due to the elevated temperature and circulation of fluid. In a long-term [900 hours (38 days)] test at room temperature, Polak et al. (2004) observed slow permeability reductions in a limestone fracture subjected to groundwater flow. Following that, distilled water was flowed over 600 hours, causing permeability reduction greater than for groundwater, but then the permeability increased quickly because of the formation of wormholes. In an experiment over 900 hours and a range of temperatures up to 150˚C using fractured novaculite, Polak et al. (2003) observed reductions of the hydraulic aperture by a factor of 6. Smooth decreases in hydraulic aperture were interspersed with rapid decreases attributed primarily to breaking asperities under increased effective stress. Yasuhara et al. (2004) modeled these tests and considered the effect of pressure solution resulting in dissolution of the asperities.

The importance of fracture asperity-fluid interaction, particularly for a shear fracture in which asperities can be subjected to elevated stress is shown in these studies. How a fracture in the rock undergoes permeability reduction over time and correlations between specific rock types/mineral constituents and have not been well established. Long-duration laboratory fracture flow tests on a series of rock samples are required to better understand these correlations. Knowing how fractures in different rock types will evolve under a variety of pressure-temperature-composition conditions, thus altering existing and induced permeability, is a benefit that could allow operators to select regions that contain rock types that are more amenable to maintaining their fracture permeability, thus reducing refracturing costs at later times.

We briefly present results of four tests here, one using Stripa granite, the other using core samples from the Brady geothermal field. We describe the experimental system we use to flow water through our fractures, and the measurements made. We compute our observed changes by assuming two model geometries: parallel flat fractures, and cylindrical wormholes. In our tests, the hydraulic aperture was very strongly influenced by the system mechanical loading, and longer-term changes were likely the result of geochemistry. We present aperture measurements, and preliminary results of numerical modeling.

2. EXPERIMENTAL STUDY

Our experimental investigation examined four rock types – granite, dense metasediment, rhyolite tuff, and a lithic tuff. We performed our tests in a unique custom test apparatus. These are described below.

2.1 Description of initial core samples

Geothermally relevant core samples were selected for the hydrothermal experiments. The first sample tested was granite from the Stripa mine in Sweden. The other three samples were obtained from the Brady's BCH-3 well, courtesy of Ormat. This well is located very near the Brady's 15-12 well, which was the subject of a DOE-funded EGS field well stimulation project. A multi-stage hydraulic stimulation program was conducted in the bottom 800 feet of the 15-12 well, but no sustained enhancement of the permeability has been achieved to date.

Our **granite** sample was obtained from the Stripa mine in Sweden. Petrographic analysis of this sample (Fig. 1 top left) reveals the presence of microcline (identified by crosshatch twinning), quartz (with undulatory extinction), plagioclase, and muscovite. The granite has some alteration, with a fine-grained quartz vein cutting through the sample. A published description of this granite reports the following range of mineral abundances: quartz: 35-45%, plagioclase (partially seriticized): 35-39%, microcline: 12-24%, with minor amounts of chlorite, muscovite, biotite, and epidote (Olkiewicz et al., 1979). Figure 2 (top left) shows the approximate spatial density distribution for the granite sample using calibrated X-ray computed tomography (CT) (top left panel), with the density histogram on the right.

The three samples from the BCH-3 well were selected to represent distinct lithologies. The deepest sample is a **meta-sedimentary mudstone** from 4873.0-4873.7 feet, corresponding with the lower stimulation zone of the Brady's EGS project. This sequence was described by Lutz et al. (2011) as consisting of highly deformed to foliated fine-grained metasedimentary rocks with abundant chlorite. Petrographic examination of this sample (Figs. 1 and 2 top right) indicates that it is a fine-grained, highly altered metasediment cut by a calcite vein. Small quartz grains have undulatory extinction, and the groundmass is altered to clay and calcite. A correlative sample (DEP11) from a depth of 4863.0-4863.4 feet analyzed by TerraTek (2011) is described as a fine-grained, highly chloritic meta-mudstone with 55-61% total clay and well-defined clayey foliation planes and a sheared fabric. Figure 2 (top right) shows the approximate spatial density distribution for the granite sample from CT, with the density histogram on the right.

A second sample of the BCH-3 core used in the hydrothermal experiments was a **rhyolite ash flow tuff** collected from a depth of 3944.5 to 3945 feet. This is part of a sequence of devitrified rhyolite ash flow tuffs that are present from 3,700 feet to about 4,100 feet in the BCH-03 well (Lutz et al., 2011). Petrographic examination of a thin section from 3944.8 feet indicates that it is a crystal-rich rhyolite tuff with phenocrysts of plagioclase, quartz, biotite, and iron oxides (Figs. 1and 2 bottom right). A correlative sample (DEP4) from a depth of 3899.0-3899.4 was described by TerraTek (2011) as a devitrified rhyolite with less than 21% quartz and less than 21% total clay. XRD and QEM-SEM analyses reported by Ayling et al. (2012) for a similar rhyolite ash flow tuff sample from a depth of 3902 feet reported the following mineral abundances (QEMSCAN values listed in parentheses): quartz – 9.5 (2.5)%, micas – 5.3 (5.8)%, calcite – 14 (12)%, alkali feldspar – 6.9 (6.3)%, plagioclase – 43 (46)%, smectite and chlorite – 13 (14)%, and illite – 1.5 (1.1)%. Other detected phases (present in minor abundance) included pyroxene, zeolites, oxides, and dolomite. Figure 2 (bottom left) shows the approximate spatial density distribution from CT for the rhyolite sample, with the density histogram on the right.

The shallowest sample studied from the BCH-03 core is an **altered lithic tuff** sample from 2310 feet. This sample is part of a sequence of Oligocene ash flow tuffs described by Lutz et al., (2011). Cursory examination of the hand sample shows the presence of large (1 cm) angular lithic fragments (Figs. 1 and 2 bottom right). No petrographic examination of this sample was conducted. Samples of this core are cut by veins containing a white tabular to fibrous prismatic mineral (perhaps a zeolite). Figure 2 (bottom right) shows the approximate spatial density distribution for the lithic tuff sample, with the density histogram on the right.

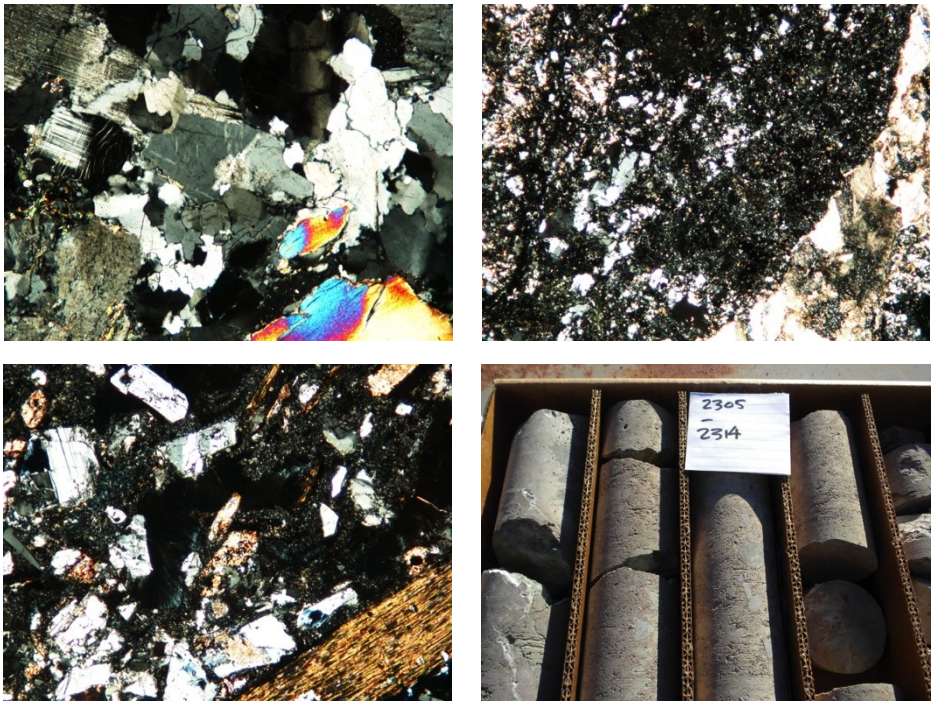

Fig. 1. top left - photomicrograph of Stripa granite under crossed nicols; top right - photomicrograph of BCH-3 metasediment from 4873.2 feet under crossed nicols. Calcite vein cuts sample on the right side. bottom left - photomicrograph of BCH-3 rhyolite ash flow tuff from 3944.8 feet under crossed nicols. Bottom side of photos is 1.75 mm. bottom right - photo of lithic tuff from BCH-03 well from the depth interval of 2305-2314 feet. Angular lithic fragments greater than 1 cm in length are present.

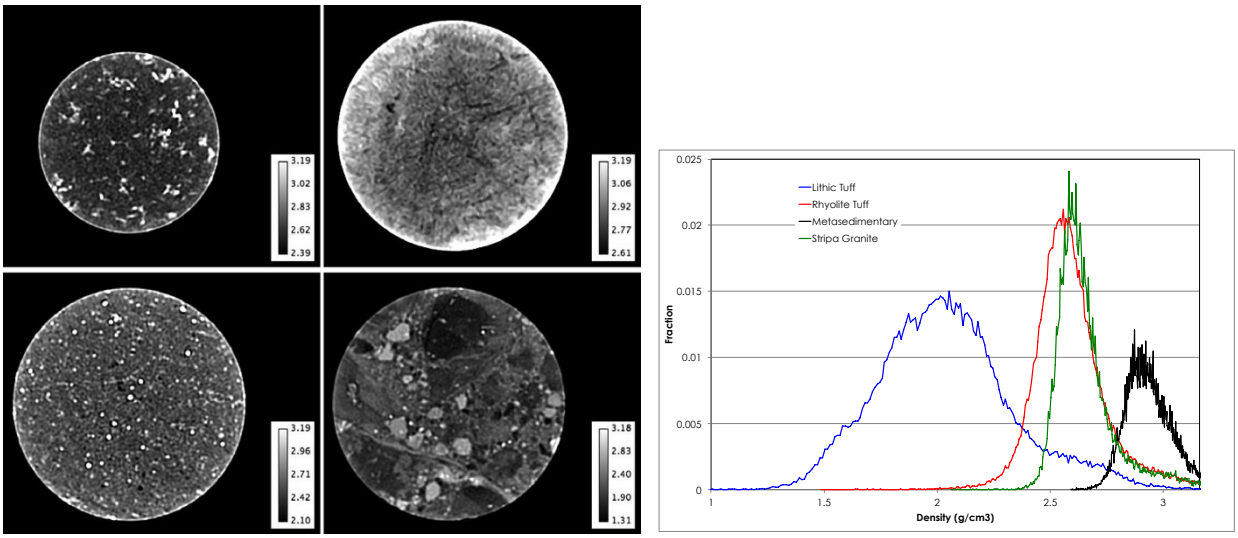

Figure 2. X-ray CT cross sections showing approximate density distributions in samples tested. top left - Stripa granite sample; top right - BCH-3 metasediment from 4873.2; lower left - BCH-3 rhyolite ash flow tuff from 3944.8 feet; lower right - BCH-03 lithic tuff from 2310 feet. Sample diameters are about 63 mm (Stripa sample is 49 mm). right – density distributions extracted from CT data.

2.2 Test apparatus and method

To perform our fracture sustainability tests, we built a custom apparatus, shown schematically in Figure 3, allowing application of a normal stress on a rock core fractured perpendicularly to the rock axis. Samples up to 5.7 cm in diameter and approximately 5 cm in length can be placed in the chamber. Prior to testing, a small diameter hole is drilled along the rock axis about 60% through the core to allow water to flow to the soon-to-be fracture, and the rock core is then fractured using a custom tool that applies a compressive stress around the circumference at the center of the core, resulting in an extensile fracture perpendicular to the core axis. This fracture is strongly impacted by heterogeneities and the grain of the rock, and our samples had strong variability in both.

The details of our custom apparatus are presented in Kneafsey et al. (2015) and summarized here for completeness. The custom pressure vessel was made from Grade 5 titanium which was cleaned and oxidized to hinder corrosion. Graphite and Kalrez were used at the top and bottom seals in different tests, and the shaft was allowed to move vertically. Custom machining allows the use of either sealing material. In the vessel, the sample rests on the titanium pedestal support, which rests on a shaft that extends through a seal in the bottom and is supported on a hydraulic jack allowing application of a normal stress on the fracture surfaces. An Active Sensors LT0951-010 high-temperature linear voltage differential transducer (LVDT) is connected to the shaft to indicate sample displacement caused by the fracture closing.

Upstream and downstream pressures and the pressure differential between the inlet and outlet are independently measured. In spite of calibration, some zero shift remains in the differential pressure measurements. This shift was measured frequently using a bypass manifold that allows isolation and equilibration of the pressure transducers, and allows checks of the upstream and downstream pressure transducers. The pressure transducers are maintained at room temperature. Room temperature affected the differential pressure measurements (~0.007 psi/C) but room temperature was fairly stable over the course of the tests. The differential pressure transducer is set to indicate differential pressures up to about 100 kPa. Pressure differentials in excess of this value are calculated using the upstream and downstream pressures.

Flow to the sample is provided using a high-pressure syringe pump. Flow to the sample passes through a temperature equalizer bath to ensure that the inlet (and outlet) tubing are kept cool, and then to the vessel and sample. Water entering the sample first flows through the cylindrical hole in the top half of the sample to the fracture, where flow resistance is governed by pressure and aperture geometry. The flow rate used was 0.01 mL/min with the exception of startup measurements. At that rate, water is heated as it moves through the pressure vessel top, and no pre-heating is used. We used distilled deionized water. After passing through the fracture, water is collected at the outer radius and flows out of the vessel, through the temperature equalizer bath, through a back-pressure regulator controlled by another high-pressure syringe pump, and is collected in aliquots using a fraction collector. We performed our tests at a fluid pressure of 10.3 MPa to maintain water in the liquid state at the experiment temperature.

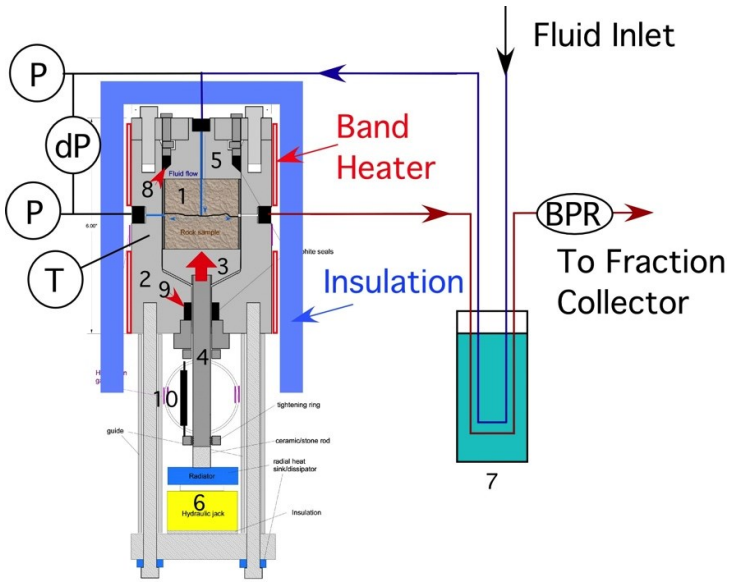

Figure 3. Experimental apparatus schematic. 1. Fractured rock sample, 2. Pressure vessel, 3. Platform, 4. Shaft, 5. Top, 6. Hydraulic jack, 7. Temperature equalizer bath, 8. Top seal, 9. Bottom seal, 10. LVDT

2.3 Test Procedure

After preparing the rock sample (machining, drilling, and fracturing), a titanium ring machined with an interference fit is heated, placed over a sample half, and cooled. The outer diameter of the titanium ring fits in the vessel with a close tolerance to minimize dead volume. Holes in the ring allow for placement of pins to help maintain (mis)alignment of the two fracture halves. A profilometer was used to describe the fracture surfaces. The travel on the scanning table is less than the diameter of the cores we are using. To accommodate for this and allow the entire surface to be scanned, a second stage is fit to the original stage allowing sample placement in four relatively precise locations simplifying data stitching and registering. Upon completion of the profiling, photographing, and observation, the two samples are matched, and then an angular offset is applied and held in place using the pin. The sample is carefully installed into the vessel, and the vessel is assembled and connected to the flow system. Two 1/8 inch copper plates, formed to match the outer diameter of the vessel and the inner diameter of the heaters are placed around the vessel to enhance heat distribution, and the heaters and insulation are installed.

3. RESULTS

3.1 Pressure, Temperature, and Displacement

Pressure, temperature, differential pressure, displacement, and computed planar aperture and wormhole dimensions are presented in Figure 4. Because of the quantity of data, we will focus the discussion here on the rhyolite ash flow tuff, shown in the lower left panel.

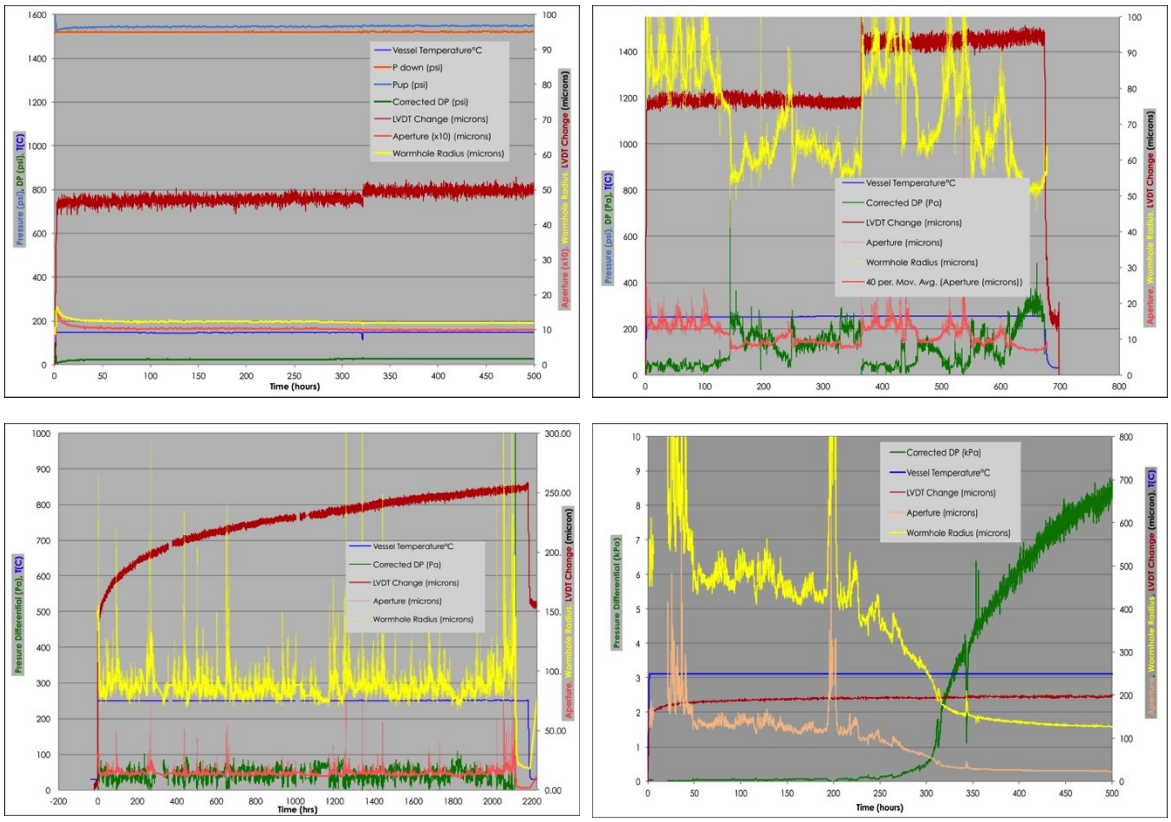

Figure 4. Pressure, temperature, differential pressure, displacement, and computed planar aperture and wormhole dimensions upper left – Stripa; upper right – metasediment, lower left – rhyolite ash flow tuff, lower right – lithic tuff. Note the line colors and the axis labels are correlated.

The test on the Stripa granite was performed at 150°C, whereas the other tests were performed at 250°C. In each of the panels in Figure 4, the green curve represents the corrected pressure differential across the sample. These data along with properties of water at the experiment conditions are used to compute the dimensions of a fictitious planar aperture and wormhole, two end members that could describe a fracture (see Kneafsey et al, 2015 for details). Errors in this measurement are compounded significantly (to the third and fourth power) in the computation of aperture or wormhole radius. Consequently, this is a very important measurement. Corrections are needed for the value the transducer reads at zero differential, and for the difference in mass of the water on either side of the differential pressure transducer do to one side having a heated (lighter) water column. For the case of the rhyolite tuff sample in the lower left panel of Figure 4, the differential pressure was very low, indicating a large aperture over several thousand hours.

The red curve in each panel of Figure 4 depicts the macroscopic closing of the fracture indicated by the LVDT. Larger relative numbers indicate the sample is becoming smaller – the aperture is collapsing. For the Stripa granite and metasedimentary rock shown in the top two panels of Figure 4, very little change in sample size occurred, with the exception of a stop-start incident in each. Each of these had a compaction of a few microns. The Stripa sample had large differential pressures over the entire course of the experiment, whereas the differential pressure in the metasedimentary rock varied in spite of the apparent LVDT-indicated stable fracture aperture. For the rhyolite ash-flow tuff and lithic tuff shown in the bottom two panels, there is more sample compaction. In the lower left panel describing the test with the rhyolite ash-flow tuff, there is significant compaction (100 or more microns), but no change in differential pressure. This indicates that the aperture was too large to affect the measured pressure differential in spite of the compaction. Changes in the aperture were observed also showing continued elevated permeability. For the lithic tuff, the compaction was smaller than the rhyolite case, however the impact on differential pressure indicating a significant loss in permeability is clear. No obvious correlation between compaction and permeability was observed.

3.2 Surface profilometry and aperture calculations

Surface profiles were measured using a Nanovea PS-50 optical profiler before and after fracture sustainability testing. Data were further processed using ImageJ software (Rasband, W., ImageJ 1.50e, imagej.nih.gov/ij). When using the profilometer, the scan data are collected for overlapping quarters of the rock face at four different scan heights. The data are then normalized and stacked using a Matlab scrip, and then the resulting compiled quarter data are stitched together in ImageJ using the pairwise stitching plugin (Preibisch

et al. 2009) to make a circular profile surface. The circular fracture surfaces from each face, top and bottom from pre- and post-test were registered to align them and then subsequently subtracted from each other to estimate aperture and changes to the topography of the surfaces.

Figures 5 and 6 show the stitched results of the profilometry for the rhyolite ash flow tuff sample. Figures 5a and b show the top half of the fracture before and after the test, and Figure 5c shows the difference between the profiles. Figures 5 d, e, and f show the same for the bottom half of the fracture. The slight differences between the four quarters can be seen in (c) and (f) and further work is needed to improve where data overlaps. Resulting differences do show, however, that the bottom half of the fracture exhibits more variance between the pre- and post-test. Figure 5g is a color photo of the bottom half of the fracture showing an obvious red-toned stain.

Apertures were estimated by registering the surfaces (top and bottom) both for the pre-test, and also for the post-test. The top profile was then flipped horizontally and inverted to mirror the bottom surface, and the maxima from each surface was matched. The values for the bottom surface were then subtracted from the top surface to measure aperture distribution. This was repeated for multiple rotations of the top rock surface as related to the bottom rock. During the fracture sustainability flow test, the rock surfaces were rotated 2 degrees relative to the original fracture orientation.

When subtracting the top from the bottom pre-test data, the aperture distribution was smoothly distributed, but as the rotation angle increased from the original position the aperture size increased and the size distribution widens (Figure 6 top left). For the post-test, the average size of the aperture is larger and rotation of the surfaces does not correlate strongly to aperture size, indicating that the surfaces no longer fit as closely together as they did when the fracture was newly created (Figure 6 top right). In addition, the aperture distribution for the post test sample has a bimodal distribution. A typical aperture map of the pre-test is shown in Figure 6 (bottom left panel) and of the post-test in Figure 6 (bottom right panel) showing a widening (brightening) of the aperture.

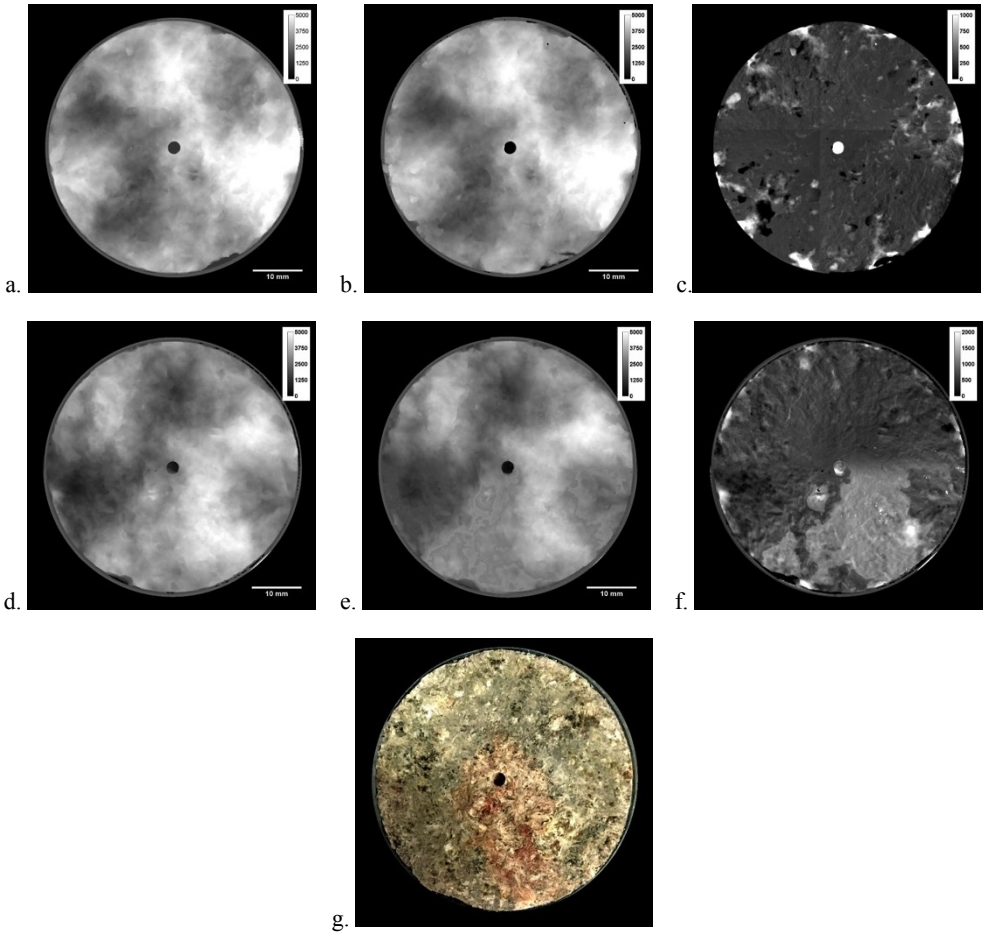

Figure 5. Surface profiles for the rhyolite tuff sample. a. - top half of the fracture before; b. - top half of the fracture after the test; c. - difference in top resulting from test; bottom half of the fracture before; d. - bottom half of the fracture after; e. –f. – differences in bottom resulting from test, g. photo of bottom half following test.

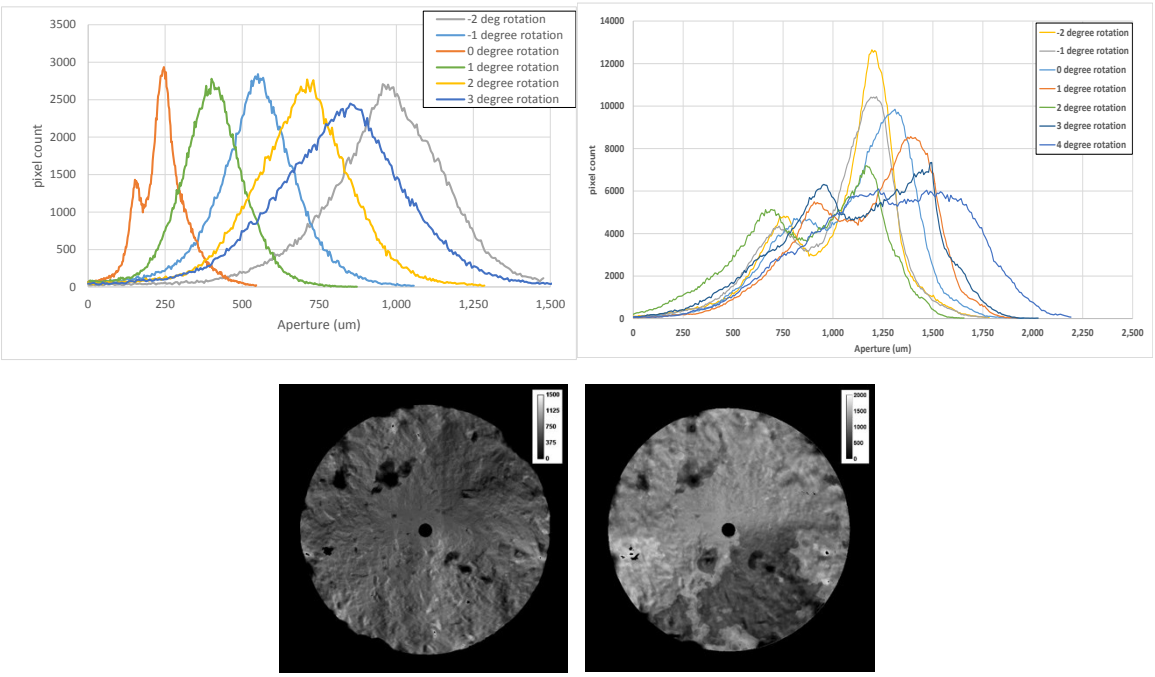

Figure 6. Aperture distributions for different rotations. top left – pre-test; top right – post-test, bottom left – pre-test aperture distribution; bottom right – post test aperture distribution

3.3 Water Chemistry

Water samples were collected by an automated sample collection system (Frac-920, General Electric), which was programmed to collect a composite 6 hr sample under open laboratory conditions, which at the experimental flow rate of 0.01 mL/min averaged at 3.6 mL/sample. Input fluid was deinonized water (MilliQ Elix, Millipore, 18 mΩ), which was measured independently and shown to have no detectable anions, cations, or Si (data not shown). Cations in the effluent samples were analyzed on a Perkin Elmer Elan DRC II ICP-MS instrument after being acidified and diluted with 2% ultrapure HNO_3 acid. Ammonia gas was used as the reaction gas in the Dynamic Reaction Cell of the Elan DRC II ICP-MS instrument to remove isobaric interference from Argon carrier gas and sample matrix, especially for the analysis of Fe, Ca and K elements. A mixture of Li6, Sc, Ga, Tm and Rh solution was used to provide the internal standards and was spiked into both the calibration standards and effluent samples to correct for any potential instrument drift during sample analysis. The anions were analyzed on a Thermofisher Dionex 2100 IC instrument equipped with an IonPac AS 11 analytical column. The analysis was performed under isocratic mode with 30mM KOH as the mobile phase at a column temperature of 30 °C. Samples were diluted 5 to 12 times with ultrapure D.I. water before being analyzed on the IC instrument.

Strict mass and charge balances were not possible for the experiments because we were not able to monitor bicarbonate due to the design of the fluid collection system. A blank system sample was run using a Ti plug in place of the rock core, after the other rock samples were completed, and showed some contamination from Al, Si and F. The Si and Al may have been from precipitation from previous samples, and the F was likely from degradation of sealant materials. Al could also have been derived from the Ti alloy. As a result, we are still assessing the data. Concentrations tended to spike early in the experiment before reaching steady-state. Several species, such as Cl, could not have come from contamination, and yield important data regarding deformation of the sample. For example, in the rhyolite (3900 foot depth), Cl concentrations increased over the first few days, reached a peak, and then declined to very small values during the "steady-state" period. Integrating under the Cl-time curve, and using the published porosity of 0.0345, with the flux of 0.01 ml/min gives a pore water Cl concentration of ~ 16,900 mg/liter. Therefore, Cl concentrations indicate that the core was saturated in brine at concentrations about an order of magnitude higher than the reservoir Cl concentrations at Brady's and about 5 times higher than at Desert Peak. Given the time history of the Cl, it appears that it was partially squeezed out of the sample consistent with the observed vertical shortening.

3.4 Description of the surface of the fractures after the experiment via scanning electron microscopy/ energy dispersive X-ray spectroscopy (SEM/EDS)

The surface of the fractures after the experiment all display both weathering features and precipitation of newly formed phases. The weathering involves mainly the plagioclases, which are andesine/labradorite, for the meta-sedimentary rock, rhyolite ash-flow tuff, and altered lithic tuff samples, and for the Stripa sample a more sodic composition, close to pure albite is found. Calcite, showing weathering structures, is present in the meta-sedimentary rock sample as well. The chemistry of the plagioclase, and the availability of calcium in general, apparently seems to significantly affect the crystallization of the new phases, where in the Brady samples we can observe the growth of calcium zeolites, high in aluminum, such as phillipsite and calcium-faujasite, whereas in the Stripa sample the lack of calcium available and the different general chemistry triggers the crystallization of aluminum hydroxides such as diaspore.

The identification of the secondary phases by using only semi-quantitative energy dispersive X-ray spectroscopy (EDS) analysis and morphology is rather challenging. Best guesses have been provided and they seem to be compatible with all the parameters including the crystallization conditions considered.

3.4.1 Stripa Granite

Figure 7 shows SEM images highlighting dissolution and precipitation features observed as a result of the Stripa test. The dissolution of feldspar is evident in this sample, along with the crystallization of aluminum hydroxide in the form of sub-micrometric crystals of diaspora. Zeolites were not observed. No clear secondary phases containing relevant amounts of silicon were identified. Plagioclase in this sample is mostly sodic (close to pure albite), whereas andesine/labradorite are present in the Brady samples. Secondary electron (SE) images are shown, and EDS was performed on some locations to provide elemental information. Albite was observed to dissolve, and diaspora crystal aggregates precipitated during the test.

3.4.2 Meta-sedimentary rock

Figure 8 shows SE images of the post-test sample. The meta-sedimentary mudstone sample shows rather complex surface features and the identification of the secondary phases is very challenging due to the lack of diagnostic morphological features. EDS data show compatibility with calcium-rich aluminum-silicates. Dissolution features on reactive grains, mostly carbonates, are evident. Additional pre-existent phases are chlorite, biotite, and clays.

3.4.3 Rhyolite ash-flow tuff

The surface of the rhyolite ash-flow tuff sample shows areas where significant preferential dissolution of some grains happened. The observations of the residual and of the weathered crystals surfaces suggest that significant dissolution of plagioclase (andesine/labradorite) is the main process involved. Figure 9 shows SE images of the post-test sample.

We have identified calcium aluminum silicates as secondary phases, compatible in both chemistry and crystal morphology with phillipsite, more evidently than in the meta-mudstone sample. The prismatic shape with oblique termination, the presence of calcium as the main cation, and the large amount of aluminum (in addition to the crystallization conditions) suggest phillipsite. In addition to phillipsite, the precipitation of crusts extremely rich in iron (as oxi-hydroxides) and illite/smectite crystals are observed as well.

3.4.4 Altered lithic tuff

The surface features of the altered lithic tuff sample are more variable and they highlight a more complicated crystallization history than other samples. Figure 10 shows SE images and EDS results from locations on the altered lithic tuff sample. As with the other Brady samples, the dissolution of plagioclase is evident, but markedly different newly-formed phases can be found. Crystals similar to the phillipsite are observed on parts of the sample. In addition to those, new crystals with octahedral shape are present as well. Given the peculiar morphology and the chemical composition, these crystals have been identified as faujasite-calcium. Coatings rich in iron and in clays (smectite) can be found on the surface of the reacted fracture as well.

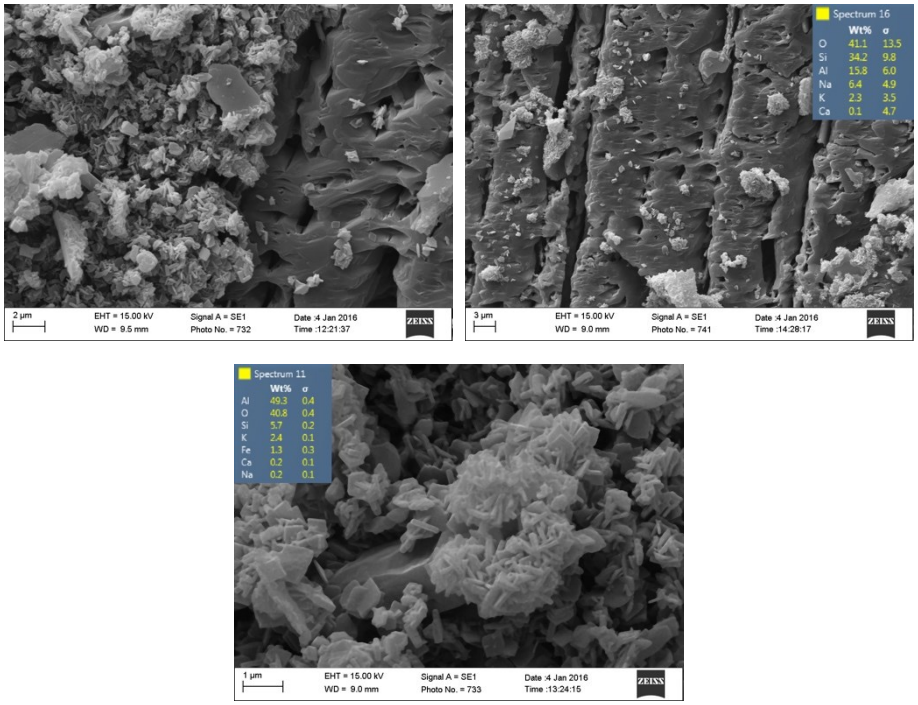

Figure 7. top left - typical Stripa sample surface featuring a weathered albite crystal (on the right) with dissolution pits, and newly crystallized diaspore rosette crystal aggregates (on the left) coating the surface; top right - SE image highlighting the dissolution pits in albite and the preferential dissolution along the boundaries of the polysynthetic twinning of the plagioclase. EDS analysis confirms a mostly sodic plagioclase; bottom - high resolution secondary electron (SE) image of the reaction products. From the EDS analysis mainly aluminum and oxygen are present, this information, coupled with the morphology of the crystals, suggests that these crystals are diaspore. No clear evidence of other phases, hosting the Na and Si derived from the dissolution of albite, has been observed.

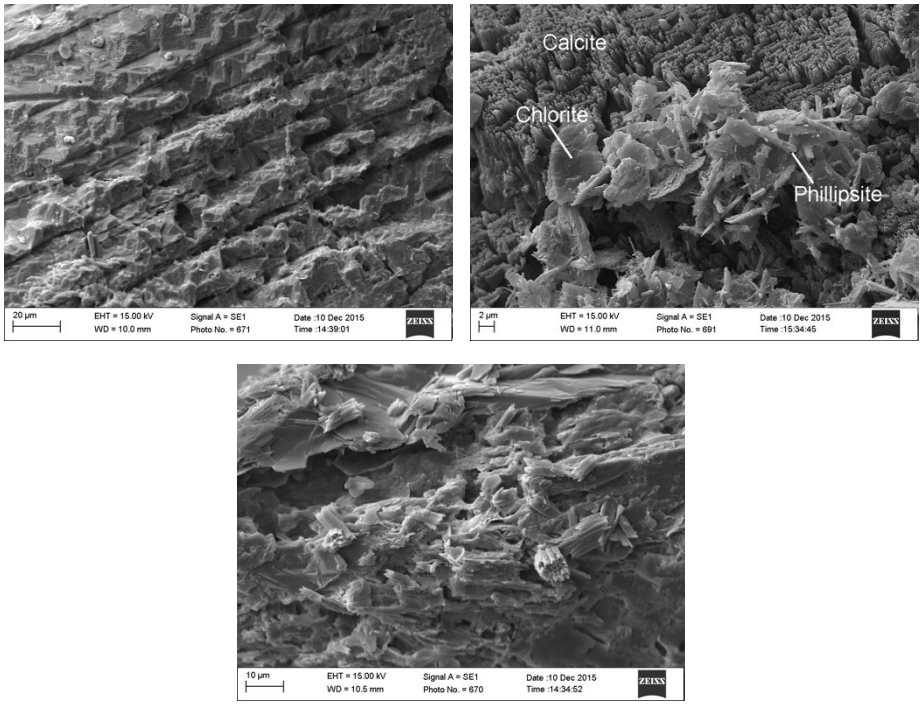

Figure 8. Meta-sedimentary rock surface. top left - SE image showing the surface of a calcite grain (identified via EDS analysis) with evident dissolution pits and enhanced dissolution along the cleavage planes of the crystal; top right - weathered calcite grain (top) and precipitation of secondary phase(s) (bottom). From the EDS analysis and the lack of clear morphological features it is not possible to give a proper identification of the new phase(s). Some platy crystals seem to be remobilized clays, while the other precipitated material seems to be weathered mica and a prismatic Calcium

aluminosilicate with a chemical composition compatible with phillipsite; bottom - thin prismatic crystals aggregates identified as apatite cover carbonates and mica grains in one part of the sample.

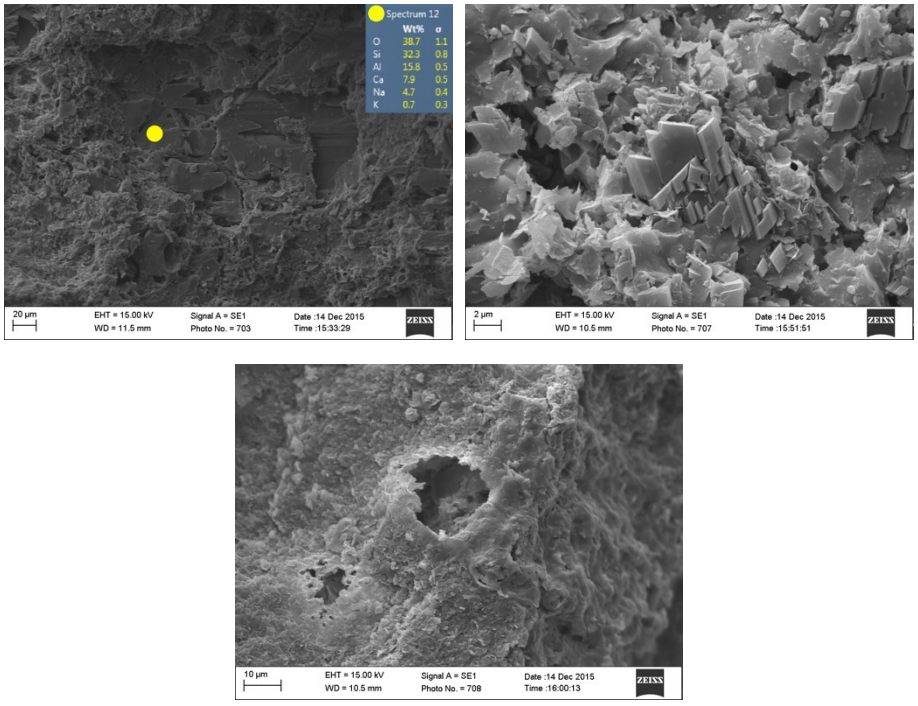

Figure 9. Rhyolite ash-flow tuff. top left - SE image showing a large plagioclase crystal with dissolution features; top right - surface covered with the phillipsite crystals (+ clays); bottom - example of coating of iron oxi-hydroxides and clays.

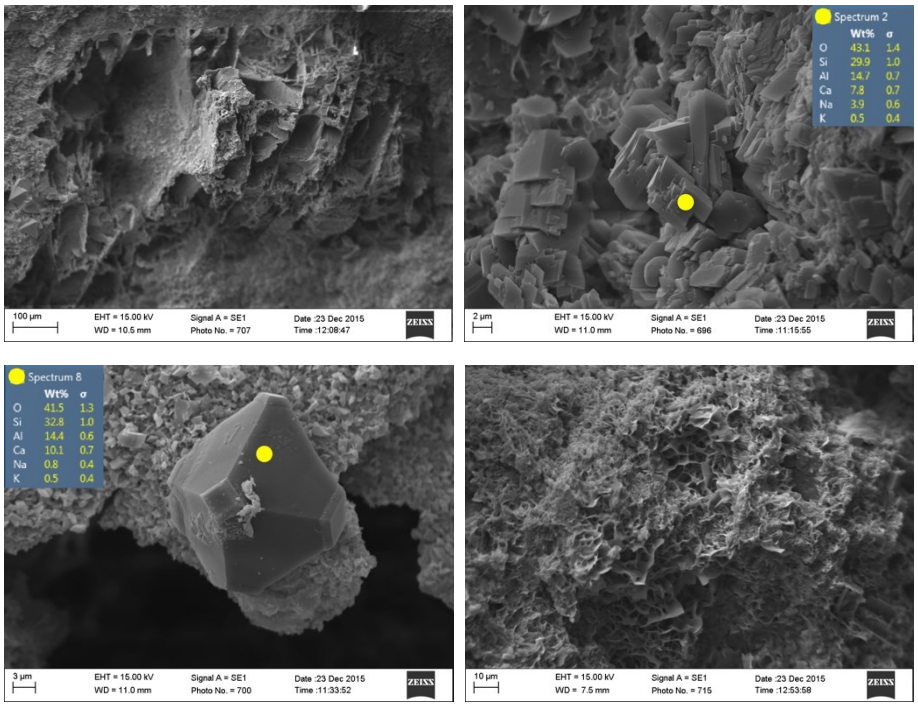

Figure 10. Lithic tuff. top left - large crystal of plagioclase showing a high degree of weathering. The original morphology is highlighted by the residual material originally deposited in between the polysynthetic twinning lamellae; top right - part of the sample with the prismatic with monoclinic termination crystals identified as phillipsite; bottom left - example of a faujasite-calcium octahedral crystal. This crystal also highlights (overgrowth) an event that disturbed the crystallization during the experiment; bottom right - coating of illite/smectite and Fe oxi-hydroxides on the surface of the fracture.

4.0 MODELING COUPLED STRESS AND FLOW, AND REACTIVE-TRANSPORT

4.1 Coupled stress and flow – Stripa sample

Initial stress and flow modeling is split in two parts: modeling of fracture closure under application of axial stress under laboratory conditions (10.3 MPa fluid pressure, 150˚C for Stripa granite, 30 MPa axial stress) for a simulated fracture surface, and geochemical (e.g., dissolution, reaction) simulation in a uniform fracture at experimental conditions (250˚C, 10.3 MPa fluid pressure).

Coupled stress and flow were modeled using TOUGHREACT/ROCMECH (J. Kim, et al., 2012, J.T. Smith, et al., 2015). This code computes flow and stress interactions using sequential coupling between flow calculations, stress calculations and chemical calculations on each time step. It is formulated for flow in porous media. Water and sample hole portions of the experiment are represented as very porous ($\phi = 0.999$) with permeability appropriate for laminar flow. Changes in pressure translate directly to changes in diagonal total stress (scaled by a Biot coefficient α_B). The code includes provision for material failure through Mohr-Coulomb conditions and tensile failure, and allows stress calculations before and after failure has occurred. Here, the artificial fracture between core segment halves is modeled as a pre-existing failure. The experiment was designed to limit all but vertical sample motion, so the fracture is treated as a tensile failure. With single tensile failure, dilation and deflation are allowed in a single direction, the direction that would be the minimum effective stress direction were the fracture artificially closed. The code was modified to allow stress (traction) and displacement boundary conditions on adjacent element surfaces (adjoining solid and water elements), to allow sample loading and unloading (time dependent stress boundary conditions), and to allow starting with non-zero initial material failure. The mechanics portions of the code are formulated for hexahedral elements, dictating grids which map to rectangular grids.

A 36 x 36 x 10 element grid was used with exterior vertices arranged on a 25.7 mm radius circle, shown in plan view in Figure 11 (left). The vertical grid extent was 45.72 mm. The outer circle of elements were defined as water elements, and are followed by a second circle of titanium elements (except for a gap at z = 0). Elements within the outer two circles were specified as rock, hole, or gap. Gap elements and rock elements were given identical mechanical properties, except that gap elements were treated as having failed in a tensile mode and were given initial failure porosities and permeabilities corresponding to their initial gap width, using the cubic law for permeability. For the nonfractured portions of the Stripa granite, permeability was negligible. With negligible permeability, the granite and titanium were taken to have Biot coefficients of 0, and gap and water elements a coefficient of 1. The granite was taken to have bulk modulus 27.84 GPa and shear modulus 24.48 GPa (G. Swan, 1977), and the titanium to have moduli of 118.69 GPa and 42.54 GPa respectively. Hole and water elements were given identical properties- for numeric reasons both were given mechanical moduli 1/1000 of that of the rock, and given a Biot coefficient of 1, so that pressure changes translate directly into changes in total stress. In each layer of elements from z = 0 upward, the 4 central elements were hole. Hole elements were given permeability 1.26 10^{-6} m^2 and water elements 10^{-6} m^2.

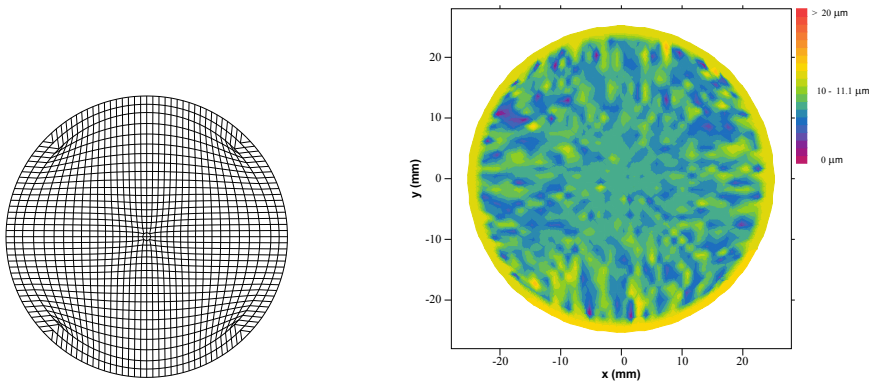

Figure 11. left - modeling mesh plan view; right - synthetic fracture aperture (unloaded) with 0.25 degree rotation and three point contact, averaged over mechanics finite elements.

For simulating fracture closure under laboratory loading, a 2-D surface was generated numerically on a 1024 x 1024 grid to have approximately a 1/f spatial spectrum, so that adjacent values are strongly correlated, with correlation decreasing with distance. The surface was scaled to have 51 micron rms topography- substantially less than the observed 3250 micron range of values measured for the Stripa core fracture surface. From this, a 724 diameter circular subset was used. This surface was turned 0.25 degrees and offset vertically to simulate the surface of the second core half. Values were averaged within elements used in mechanics finite element modeling. Closure with three-point contact was calculated. (First contact point on vertical displacement, second contact point on least rotation through any horizontal axis through first contact point, and third contact point on least additional rotation about axis through first and second contact points.) The resulting synthetic fracture had an 6.9 micron average aperture (unloaded)- much less than an inferred 400 micron opening for the measured Stripa core surfaces fitted together, but larger than an experimentally determined 4 micron hydraulic aperture for the Stripa sample under zero effective axial stress and 10.3 MPa fluid pressure (at laboratory temperature ~20 C). Unloaded synthetic fracture aperture is plotted Figure 11 (right panel), with an added ring of values in place of the separation of titanium sleeve halves.

Initial pressurization to 10.3 MPa was modeled over 10.9 seconds by injecting water in the top of the hole, not allowing displacement perpendicular to the pressure cell exterior. This results in an increase in average fracture aperture from 6.9 micron to 11.5 micron (less

than the 17 micron increase expected for the granite unconstrained by the titanium sheath). Subsequently, hole water pressure was held at 10.3 MPa and a vertical stress condition imposed on the solid elements along the cell bottom, replacing the no vertical displacement condition there. Cell bottom vertical stress was set to 10.3 MPa ramping to 30 MPa over 10 seconds. Average aperture is plotted in Figure 12, ending in a 0.87 micron average aperture. Although this is similar to an experimentally determined 0.66 micron hydraulic aperture, at this point the modeled pressure in the jacketing water elements is 13.2 MPa and outflow from the hole is less than 2 10^{-9} L/s indicating very little hydraulic connection between the hole elements held at 10.3 MPa and the exterior water jacket, despite having started with an average unloaded aperture approximately twice the experimental hydraulic aperture at zero effective axial stress. It appears that more accurate fracture surface topology is needed to reproduce the experimental variation in hydraulic aperture with axial stress.

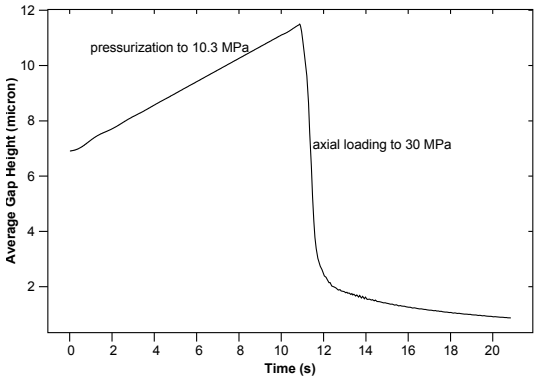

Figure 12. Average fracture aperture during pressurization and axial loading (simulated).

4.2 Reactive-transport modeling

Thermal-hydrological-chemical (THC) simulations were performed using the parallel reactive-transport code TOUGHREACT V3.20-OMP (Sonnenthal et al. 2014). The numerical grid and design of the simulation was adapted from the THM model of the Stripa granite experiment (above). Thermodynamic, and kinetic data were chosen from simulations of the Newberry enhanced geothermal system (Sonnenthal et al. 2015) and experiments on Desert Peak rhyolitic tuff. The deionized injection water was pre-equilibrated with CO_2 and O_2 at atmospheric pressure to capture the experimental conditions. The initial mineral assemblage consisted of calcite, dolomite, quartz, montmorillonite (Mg, Ca, Na, K), illite, clinochlore, plagioclase (albite-anorthite), sanidine, biotite (annite-phlogopite), apatite, and hematite. All minerals were allowed to dissolve/precipitate under kinetic constraints. The rhyolite core was given a porosity of 0.0345, and a permeability of 10^{-18} m^2. The initial pore water was assumed to have 0.1M NaCl based on observations of elevated Cl- concentrations in effluent over the early part of the experiment, consistent with typical reservoir salinities observed in geothermal reservoirs in this area. After 28 days, the simulation shows predominantly dissolution of all primary minerals and increasing permeability (Fig. 13), owing to the relative high fluid flux, small reactive surface area, and dilute injection water. Fluid flux distributions show predominantly flow in the hole and in the main fracture, as expected. Calcite and dolomite dissolve preferentially around the hole. The simulations have not yet considered mechanical effects on porosity or permeability, other than pore compressibility.

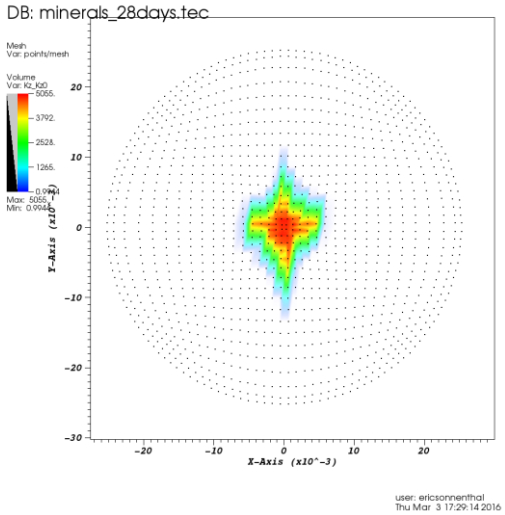

Figure 13. Simulated permeability ratio ($k_z/k_{z,initial}$) from THC model after 28 days injection. Strong dissolution led to permeability increases near center hole.

CONCLUSIONS

We have observed a wide range of behaviors in our tests, from low permeability and low permeability change with dissolution and precipitation (Stripa granite) to large compaction with limited permeability change (rhyolite). Both of these types of measurements are indicative of fracture behavior and sustainability. For example, the rhyolite sample had the largest initial aperture of all samples tested, and in spite of no observed permeability change, showed the largest compaction. A longer term test might have showed closure of the fracture. The meta-sedimentary mudstone test showed variable permeability, in spite of very little indicated fracture closure from compaction. This may be indicative of some movement of fines in the aperture. The greatest change in permeability was indicated in the lithic tuff, although the compaction was not as significant as the rhyolite.

Using distilled water as the fluid, dissolution was expected. Surprisingly, although the hydraulic residence time was small, several minerals were observed to precipitate. The minerals observed to precipitate formed small-high-surface area grains or plates. None of these appear to be minerals that are mechanically supportive and all appear to be detrimental to permeability. The lack of mechanical strength might indicate that upon the dissolution or deformation of asperity contacts, the zones containing these minerals would be easily compressed, causing significant declines in permeability.

We have viewed our flow property changes using parallel-plate aperture or a wormhole end members. Neither of these two end members adequately describes flow in a real heterogeneous fracture. Wormholes would be less susceptible to mechanical closing, however are poor at exchanging heat, whereas the reverse is true for parallel-plate aperture. Nonuniform dissolution along an active flow path in a fracture would tend to produce wormholes. We have not seen this happen yet, however the duration of our tests may be too short for this to happen.

Aperture observations have shown both little change, and change that indicates the future formation of a worm-hole like high-permeability pathway. Further analysis of the initial and final conditions is needed to understand this better. Continued modeling of the tests is underway. This modeling is adding to our understanding of the complex nature of the sustainability of fractures. This seems to be affected by the initial geometry of the asperity contacts as well as the mechanical and chemical processes. In addition to questions identified in the experimental work, modeling will refine and provide additional questions and answers that will aid in the understanding of fracture and reservoir sustainability. In spite of the short flow pathway through our samples, mineral precipitation occurred in each test. Longer pathways would provide a better quantification of the spectrum of reactions that will occur.

ACKNOWLEDGMENTS

This work was supported by the Assistant Secretary for Energy Efficiency and Renewable Energy (EERE), Office of Technology Development, Geothermal Technologies Program, of the U.S. Department of Energy under Contract No. DE-AC02-05CH11231. The meta-sedimentary, rhyolite and lithic tuff rock core samples and composition information were provided by Ormat Technologies, Inc.

REFERENCES

1. Ayling, B., Rose, P., Petty, S., Zemach, E., and Drakos, P. (2012) QEMSCAN® (Quantitative evaluation of minerals by scanning electron microscopy): Capability and application to fracture characterization in geothermal systems. Proceedings, 37th Workshop on Geothermal Reservoir Engineering, Stanford University, SGP-TR-194, 11 p.
2. Auradou, H., Drazer, G., Boschan, A., Hulin, J-P., and Koplik, J. (2006), Flow channeling in a single fracture induced by shear displacement, Geothermics, 35(5 - 6), 576-588.
3. Chen, Z., Narayan, S.P., Yang, Z., and Rahman, S.S. (2000), An experimental investigation of hydraulic behaviour of fractures and joints in granitic rock, International Journal of Rock Mechanics and Mining Sciences, 37(7), 1061-1071.
4. Davatzes, N.C. and S. H. Hickman (2010), The Feedback Between Stress, Faulting, and Fluid Flow: Lessons from the Coso Geothermal Field, CA, USA, Proceedings World Geothermal Congress 2010, Bali, Indonesia, 25-29 April 2010
5. Fetterman, J. A. and N.C. Davatzes (2011), Evolution of Porosity in Fractures in the Newberry Volcano Geothermal System, Oregon, USA: Feedback between Deformation and Alteration, GRC Transactions, 35, 339-346.
6. Gentier, S., Lamontagne, E., Archambault, G., and Riss, J. (1997), Anisotropy of flow in a fracture undergoing shear and its relationship to the direction of shearing and injection pressure, International Journal of Rock Mechanics and Mining Sciences, 34(3 - 4), paper 094.
7. Kim, J, E. Sonnenthal, J. Rutqvist, 2012. Formulation and sequential algorithms of coupled fluid/flow and geomechanics for multiple porosity materials, Int. J. Numer. Meth. Engng, 92, 425-456.
8. Kneafsey, T. J., S. Nakagawa, P. F. Dobson and B. M. Kennedy (2015). Fracture Sustainability in EGS Systems – Results of Laboratory Studies. Fourtieth Workshop on Geothermal Reservoir Engineering. Stanford University, Stanford, California, Stanford University**:** 676-684.
9. Kneafsey, T.J., S. Nakagawa, P.F. Dobson, B.M. Kennedy, J.P. Icenhower, and S. Nakashima, Sustainability of Fractures in EGS Systems – A Laboratory Investigation, PROCEEDINGS, Thirty-Ninth Workshop on Geothermal Reservoir Engineering, Stanford University, Stanford, California, February 24-26, 2014
10. Lutz, S.J., Zutshi, A., Robertson-Tait, A., Drakos, P., and Zemach, E. (2011), Lithologies, hydrothermal alteration, and rock mechanical properties in wells 15-12 and BCH-3, Bradys Hot Springs geothermal field, Nevada. Geothermal Resources Council Transactions, 35, 469-476.
11. Lutz, S.J., Zutshi, A., Robertson-Tait, A., Drakos, P., and Zemach, E. (2011) Lithologies, hydrothermal alteration, and rock mechanical properties in wells 15-12 and BCH-3, Bradys Hot Springs geothermal field, Nevada. Geothermal Resources Council Transactions, 35, 469-476.
12. Nemoto, K., N. Watanabe, N. Hirano, and N. Tsuchiya (2007), Evaluation of Flow Anisotropy Within a Simulated Shear Fracture Under Stress Conditions from Shallow to Deep Reservoirs, GRC Transactions, 31, 301-306.

13. Polak, A., Elsworth, D., Liu, J., and Grader, A.S. (2004), Spontaneous switching of permeability changes in a limestone fracture with net dissolution, Water Resour. Res., 40(3), W03502.
14. Polak, A., Elsworth, D., Yasuhara, H., Grader, A.S., and Halleck, P.M. (2003), Permeability reduction of a natural fracture under net dissolution by hydrothermal fluids, Geophys. Res. Lett., 30(20), 2020.
15. Roth, J. N.C. Davatzes, A.E.Krull Devatzes, Investigating the Volume and Structure of Porosity in Fractured and Unfractured Rock From the Newberry Volcano, Oregon, USA: Evaluation of Two- and Three-Dimensional Methods, GRC *Transactions*, Vol. 37, 2013
16. Olkiewicz, A., Gale, J.E., Thorpe, R., and Paulsson, B. (1979) Geology and fracture system at Stripa. Swedish-American cooperative program on radioactive waste storage in mined caverns in crystalline rock. Technical Information Report #21, LBL-8907, 164 p.
17. Preibisch, S. S. Saalfeld, and P. Tomancak, Globally optimal stitching of tiled 3D microscopic image acquisitions, Bioinformatics (2009) 25 (11): 1463-1465 first published online April 3, 2009 doi:10.1093/bioinformatics/btp184
18. Smith, J.T. E.L. Sonnenthal, T. Cladouhos, 2015. Thermal-hydrological-mechanical modelling of shear stimulation at Newberry Volcano, Oregon, Amer. Rock Mech. Assn. 49th US Rock Mechanics/Geomechanics Symposium proceedings, 15-0680.
19. Sonnenthal E.L., Smith, J.T., Cladouhos, T., Kim, J., and Yang, L. (2015). Thermal-Hydrological-Mechanical-Chemical Modeling of the 2014 EGS Stimulation Experiment at Newberry Volcano, Oregon. In Proceedings, Fortieth Workshop on Geothermal Reservoir Engineering Stanford University, Stanford, California, SGP-TR-204.
20. Sonnenthal, E.L., Spycher, N., Xu, T., Zheng, L., Miller, N., Pruess, K. (2014). *TOUGHREACT V3.0-OMP*, http://esd.lbl.gov/research/projects/tough/software/toughreact.html.
21. Swan, G., 1977. The Mechanical Properties of Stripa Granite, September, 1977, KBS Teknisk Rapport 48, Karnsbranslesakerht, reprinted as L.B.L. Report 7074, August,
22. TerraTek (2011) Petrologic evaluation of selected core samples – Bradys Hot Springs well BCH-03 – Churchill County, Nevada. TR11-403371.
23. Yasuhara, H., Elsworth, D., and Polak, A. (2004), Evolution of permeability in a natural fracture: Significant role of pressure solution, J. Geophys. Res., 109(B3), B03204.